Role of complex energy landscapes and strains in multiscale inhomogeneities in perovskite manganites

K. H. Ahn* and T. F. Seman†
Department of Physics, New Jersey Institute of Technology, Newark, New Jersey 07102, USA

T. Lookman and A. R. Bishop
Theoretical Division, Los Alamos National Laboratory, Los Alamos, New Mexico 87545, USA
(Received 5 July 2013; published 17 October 2013)

We analyze the essential role played by complex energy landscapes in the nanometer- to micron-scale inhomogeneities observed in perovskite manganites using a model expressed in terms of symmetrized atomic-scale lattice distortion modes. We also examine the stability of large metal and insulator domains in the absence of defects. Our results demonstrate that an intrinsic mechanism, which involves long-range interactions between strain fields, the Peierls-Nabarro energy barrier, and complex energy landscapes with multiple metastable states, rather than an extrinsic mechanism such as chemical randomness, is responsible for the inhomogeneity in perovskite manganites.

DOI: 10.1103/PhysRevB.88.144415 PACS number(s): 75.47.Gk, 64.60.My, 64.70.K−, 61.50.Ah

I. INTRODUCTION

Multiscale inhomogeneity observed in perovskite manganites has been the subject of intense studies.[1] Unlike inhomogeneities for other complex electronic systems, such as stripes in high-T_c cuprates, the coexistence of metallic and insulating phases within the same crystals of manganites has been directly observed through various high-resolution local probes, such as dark field images and scanning microscopy.[2–4] Nanoscale inhomogeneities have also been implied based on x-ray diffraction results.[5] Even though some degree of phase coexistence is expected in materials with first-order phase transition, the phase coexistence in manganites is unique in its appearance over wide ranges of conditions, temperatures, and length scales from nanometer to micrometer.[1] Furthermore, understanding the metal-insulator phase coexistence and its response under magnetic fields is considered essential for the development of the theory of colossal magnetoresistance (CMR) effects of several orders of magnitude in manganites, because experimental results indicate that such CMR effects occur through percolative transitions.[2] Therefore, as a prerequisite for the CMR theory, the origin of the phase coexistence itself needs to be understood and has been one of the most controversial issues for manganites research. Theories based on chemical randomness and electronic phase separation have been proposed as a mechanism for such inhomogeneities.[6,7] However, the theory based on chemical randomness assumes an unrealistic exact degeneracy between metallic and insulating phases,[7] the correction of which ultimately leads to a homogeneous phase.[8] Also, in the early theory[6] based on a scenario of electronic phase separation into two phases with different electron concentrations, the effect of the long-range Coulomb interaction, which could be the most important term against the electron density inhomogeneity, has not been incorporated adequately into the model. Later theories[9] indicate that the long-range Coulomb interaction reduces the length scale of the electron density inhomogeneity down to nanometer scale.

As an alternative to these theories, we have previously proposed an *intrinsic* mechanism for phase coexistence,[10,11] in which the interaction between strain fields plays an important role, as recognized in earlier works.[12–14] Specifically, our model[10] includes an intrinsic complexity of energy landscapes,[15] long-range anisotropic interaction between strain fields, and discreteness of lattices, and it demonstrates how they give rise to multiscale inhomogeneities observed in manganites. In our theory, the several-orders-of-magnitude CMR effect is considered due to the change in the energy landscape by magnetic fields. This idea is supported by experimental results,[16] which show that the ground state changes from a distorted charge-orbital ordered antiferromagnetic insulating state to an undistorted ferromagnetic metallic state by 2–5 T magnetic fields. These experimental results suggest that the energy difference between the competing phases should be only about a few meV per Mn ion. Such a small energy difference between the insulating and metallic phases is surprising, and is a consequence of strong coupling between spin, charge, orbital, and lattice degrees of freedom and the experimental capability to tune the energy balance finely through doping. Our theory not only provided insights for many puzzling experimental results obtained by that time,[2–4,17,18] but it has also contributed to drawing intense research interests in the relation between strain, phase coexistence, and energy landscapes.[19] For example, the observed large-scale inhomogeneity of the order of 10 μm without any observable chemical inhomogeneity at a length scale of 0.5 μm or larger is consistent with the intrinsic mechanism.[20] The lamellar morphology of coexisting phases and the change of domain configurations upon thermal cycling between 10 and 300 K further support our mechanism based on intrinsic energy landscapes.[21] It is also found that the anisotropic epitaxial strain in thin films gives rise to anisotropic percolation, which suggests that the phase coexistence is much more strongly affected by long-range strain rather than by local chemical inhomogeneity due to doping.[22]

Furthermore, as we will show in the current paper, the atomic-scale model used in our previous work, instead of a traditional continuum model such as a phase field model,[23,24] is essential to explain the stability of the metal-insulator coexistence in the absence of defects, because the atomic-scale

energy barrier initially proposed by Peierls and Nabarro[25] blocks a parallel shift of the metal-insulator interface. Therefore, even though a continuum theory could include anisotropic long-range interaction, such a continuum theory would not support the stable metal-insulator coexistence for which two phases have different energies unlike twin structures.

We proposed the basic ideas in Ref. 10, but now we develop them further and describe more extensive implementations of the approach here. Specifically, we present details of our model, methods, and results, as well as further simulations on the stability of phase coexistence. In Sec. II, the details of the Hamiltonian used for the simulations and results obtained with various initial conditions and parameters are presented. We also contrast these results with simulations for a system that includes short-range interactions only. In Sec. III, we discuss the mechanism underlying the stability of micron-scale phase coexistence through further simulations and analyses. In Sec. IV, we summarize our main results. Definitions of symmetry modes, constraints, and relations among modes and displacements in reciprocal space are presented in Appendix A. Energies and energy gradients used for the simulations of inhomogeneous states are presented in Appendixes B and C, respectively. The programs used for the simulations are available online.[26]

II. MODEL FOR STRAIN-INDUCED METAL-INSULATOR PHASE COEXISTENCE

A. Properties of manganites, requirements for phase coexistence in manganites, and hypothesis to examine

Perovskite manganites typically have the chemical formula of $R_{1-x}A_xMnO_3$, where R represents rare-earth elements, such as La, Nd, and Pr, and A represents alkaline-earth metal elements such as Ca and Sr.[1,27,28] Important electrons for both electronic properties and structures are e_g electrons on the Mn ions, as the degeneracy of the e_g orbitals leads to a strong Jahn-Teller electron-lattice coupling. Shortly after the discovery of CMR in these materials,[29] the importance of the strong electron-lattice coupling was pointed out to explain the thousandfold CMR effect in terms of polaronic-to-metallic phase transition.[28] The same strong electron-lattice coupling is also responsible for a large structural difference between the low-temperature metallic and insulating phases of manganites. In the insulating phase, the e_g electrons are localized and the charge and orbital states are ordered. Due to the Jahn-Teller coupling, such a charge-orbital ordered state accompanies uniform and short-wavelength lattice distortions. For example, the long Mn-O bond (or the elongated e_g electron orbital) in $La_{0.5}Ca_{0.5}MnO_3$ alternates its direction within a plane, which gives rise to short-wavelength lattice distortions.[30,31] Along the direction perpendicular to this plane, the short Mn-O bond repeats itself, and therefore the unit cell is compressed along this orientation, giving uniform or long-wavelength lattice distortions. In contrast, manganites in the metallic ground state have a structure close to an ideal cubic perovskite structure without the Jahn-Teller lattice distortions because the e_g electrons are delocalized. The ground state can be changed between metallic and insulating phases in various ways, such as by the size of R and A ions, applied magnetic fields, or applied pressures.[32–34]

We propose that the first key to understanding the phase coexistence in manganites is metastability, which has been observed in many experiments. For example, the distorted insulating phase of manganites can be transformed into the undistorted metallic phase by either x rays[35] or magnetic fields,[32] and the metallic phase does not revert to the insulating phase even after the external perturbations are removed. In particular, in the x-ray experiment,[35] a reduction of superlattice peak intensity and a simultaneous increase of conductivity, while the sample is exposed to x rays, demonstrate the transformation of the insulating phase into the metallic phase and the presence of inhomogeneity. However, an energy landscape with local and global energy minima is not sufficient to explain the observed submicron scale inhomogeneity, because such inhomogeneity is unstable against thermal fluctuations. Furthermore, as mentioned above,[1] the inhomogeneity in manganites is unusual in its appearance over wide ranges of conditions and length scales, which is an indication of an extra mechanism at play that affects the phase coexistence.

Based on the strong electron-lattice coupling mentioned above and experiments showing the important role of strain in the metal-insulator transition in manganites,[36] we propose that the extra mechanism should be related to the long-range anisotropic interaction between strain fields. It is thus essential to consider the energy landscape in terms of lattice distortion variables, which will ultimately have a bearing on other degrees of freedom such as magnetic moment or electron density. The origin of the long-range anisotropic interaction within this framework is bonding constraint, often referred to as strain compatibility, which enforces single-valued strain fields without broken bonds.[37–40] The anisotropy reflects discrete rotational symmetries associated with lattice structures.

The cubic phase of perovskite manganites contains five atoms per unit cell. The insulating charge and orbital ordered phase consists of a zigzag pattern of the long Mn-O bond orientation, which further increases the number of atoms per unit cell. Inclusion of such details is necessary for a complete description of the properties of these materials. For the current study, however, we focus on the following three key features of manganites essential for multiscale inhomogeneities, and we capture them in a simple model. First, the metallic phase has almost no lattice distortions in comparison with the charge-orbital ordered insulating phase. Second, the insulating ground state has a uniform or long-wavelength lattice distortion. This property is essential because it is the long-wavelength distortion, not the short-wavelength one, that gives rise to the long-range anisotropic interaction between strain fields. Third, the insulating phase has a short-wavelength lattice distortion, in addition to the uniform distortion. As we will show below, the symmetry-allowed coupling between the uniform and short-wavelength distortions gives rise naturally to an energy landscape with multiple minima. Our hypothesis is that any system with these three properties could host metal-insulator phase coexistence. Our goal is to find a simple model system and verify this hypothesis through numerical simulations.

B. Model system, variables, and constraint equations

Before we introduce our model, we examine whether a simpler two-dimensional model can be used instead of a

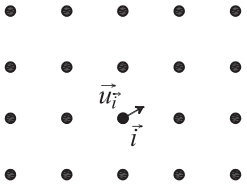

FIG. 1. Two-dimensional square lattice with a monatomic basis. $\vec{u}_{\vec{i}}$ represents the displacement of the atom at the site with the index $\vec{i} = (i_x, i_y)$, where the integers i_x and i_y range from 1 to N. The site at the bottom left corner is chosen for $\vec{i} = (1,1)$.

three-dimensional model, in particular to capture the effect of the long-range strain-strain interactions. In D-dimensional space ($D = 2$ or 3), the anisotropic strain-strain interaction decays as $1/r^D$, where r represents the distance between two points.[37,38,41] Spatial integration of $1/r^D$ would give rise to a logarithmic divergence in both two- and three-dimensional spaces,[42] which indicates that the effect of the interaction would be similar for both cases. Indeed, simulations in two- and three-dimensional spaces show similar results.[37,41,43] Thus, we limit ourselves in this work to a two-dimensional model for simplicity.

One of the simplest lattices in two-dimensional space is a square lattice with a monatomic basis shown in Fig. 1. By considering one isotropic electron orbital per site and nearest-neighbor electron hopping, the lattice supports a metallic electron density of states (DOS) without a gap. Therefore, such an undistorted square lattice shares the first property of manganites mentioned above. To include the second property, we deform the square unit cell of the lattice to a rectangular unit cell, either along the horizontal or vertical direction. To include the third property, we incorporate (π,π)-type displacements of atoms along the horizontal (vertical) direction for the rectangular lattice elongated along the vertical (horizontal) direction. Rectangular lattices with such short-wavelength lattice distortions support an electron DOS with a gap at the center, as previously obtained by Ono and Hamano,[44,45] if we consider natural electron hopping amplitude modulation by changes in interatomic distances. Therefore, such lattices have an insulating DOS for the electron density of half an electron per site. Even though the two-dimensional lattice described above is simple, it shares all three properties of manganites that we propose as essential characteristics for the observed inhomogeneity, and it provides a testing ground for our hypothesis.

We look for an energy expression for which the undistorted and distorted lattices described above are the local and global energy minimum states. For this purpose, we use symmetrized atomic-scale lattice distortion modes that we developed recently,[39] instead of displacement variables. These modes are ideal to describe anharmonic energy landscapes with multiple minima, similar to the Ginzburg-Landau theory for continuum. The symmetrized atomic-scale lattice distortion modes for the monatomic square lattice are shown in Fig. 2. The first three modes are long-wavelength modes, since they can be obtained by uniformly deforming the square lattice. The last two modes, which correspond to (π,π) staggered distortions of the lattice, are short-wavelength modes. For the square lattice, each atom is shared by four neighboring plaquettes,

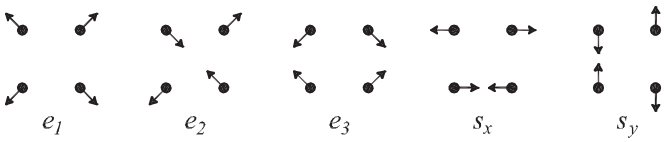

FIG. 2. Symmetry distortion modes[10,39] for the motif of the two-dimensional square lattice with a monatomic basis shown in Fig. 1.

which makes the modes at neighboring plaquettes dependent on each other. Such a constraint can be expressed in terms of equations in the Fourier transformed space, and the five modes can describe any lattice distortion for the square lattice. In the long-wavelength limit, the three long-wavelength modes become identical to the familiar strain modes, which makes our approach ideal for describing nano- and micrometer-scale inhomogeneities within the same theoretical framework. The inclusion of constraints allows our method to automatically generate the effects of the long-range anisotropic interaction.

We consider $N \times N$ square lattices.[46] The displacement variables for the atom at the site $\vec{i}$ are $u^x_{\vec{i}}$ and $u^y_{\vec{i}}$. The symmetry modes shown in Fig. 2 are defined for each site $\vec{i}$ in terms of $\vec{u}_{\vec{i}}$, $\vec{u}_{\vec{i}+(1,0)}$, $\vec{u}_{\vec{i}+(0,1)}$, and $\vec{u}_{\vec{i}+(1,1)}$. Periodic boundary conditions are applied to the modes. The definition of the symmetry modes, their constraint equations, and relations among modes and displacements are presented in Appendix A.

C. Total energy of the model and the Hamiltonian for electronic property calculations

In terms of the modes, we consider the following energy expression, $E_{\rm tot}$, as the total energy of the model system for metal-insulator phase coexistence:[10]

$$E_{\rm tot} = E_s + E_l + E_c, \tag{1}$$

$$E_s = \sum_{\vec{i}} \left[\frac{B}{2}\left(s_x^2 + s_y^2\right) + \frac{G_1}{4}\left(s_x^4 + s_y^4\right) + \frac{G_2}{2} s_x^2 s_y^2 + \frac{H_1}{6}\left(s_x^6 + s_y^6\right) + \frac{H_2}{6} s_x^2 s_y^2 \left(s_x^2 + s_y^2\right) \right]_{\vec{i}}, \tag{2}$$

$$E_l = \sum_{\vec{i}} \left[\frac{A_1}{2} e_1^2 + \frac{A_2}{2} e_2^2 + \frac{A_3}{2} e_3^2 \right]_{\vec{i}}, \tag{3}$$

$$E_c = \sum_{\vec{i}} \left[C_3 \left(s_x^2 - s_y^2\right) e_3 \right]_{\vec{i}}. \tag{4}$$

The first term E_s with the short-wavelength modes includes all symmetry-allowed terms up to the sixth order with positive coefficients, since we are interested in a first-order-transition-like energy landscape. The second term E_l with the long-wavelength modes up to the second order mediates the long-range anisotropic interactions. The third term E_c represents the coupling between the long- and short-wavelength modes, where the e_3 mode is coupled to the s_x and s_y modes in a symmetry-allowed form. This last term gives rise to the global energy minimum state with long- and short-wavelength distortions, in addition to the local energy minimum state without distortions. The energy expression $E_{\rm tot}$ gives rise to the energy landscape described in Sec. II B for appropriate ranges of parameter values.

To establish a connection between electronic properties and lattice distortions as observed in manganites, the following Su-Shrieffer-Heeger (SSH) Hamiltonian[44] is used for the electronic structure calculations:

$$H_{\rm SSH} = \sum_{\vec{i}} -t_0\left[1-\alpha\left(u^x_{\vec{i}+(10)} - u^x_{\vec{i}}\right)\right](c^\dagger_{\vec{i}} c_{\vec{i}+(10)} + \text{H.c.}) - t_0\left[1-\alpha\left(u^y_{\vec{i}+(01)} - u^y_{\vec{i}}\right)\right](c^\dagger_{\vec{i}} c_{\vec{i}+(01)} + \text{H.c.}). \quad (5)$$

Here, H.c. represents the Hermitian conjugate, and we consider only one orbital per site and neglect electron spin for simplicity. The operator $c^\dagger_{\vec{i}}$ is the creation operator of an electron at site $\vec{i}$. We include the electron-lattice coupling through the renormalization of electron hopping amplitudes only, because our goal is to demonstrate a possible connection between lattice distortion and metallic or insulating properties. Full analysis of the role of electron-lattice coupling for phase coexistence would require inclusion of terms representing the direct coupling between electron density and the lattice distortion in addition to terms like Eq. (5). For example, it has been shown that the combined effects of the two kinds of electron-lattice couplings can lead to unusual types of phase coexistence.[47,48]

The SSH Hamiltonian is a Hamiltonian for independent electrons, and it can be diagonalized within a one-electron basis. Therefore, we construct an electronic Hamiltonian matrix for given lattice distortions, $u^x_{\vec{i}}$ and $u^y_{\vec{i}}$, with a basis set $\{c^\dagger_{\vec{i}}|0\rangle\}$, where $|0\rangle$ represents the state without electrons. We diagonalize the matrix numerically, and fill energy levels with electrons according to the electron density. With the lth lowest energy eigenstate represented as $|l\rangle = \sum_{\vec{i}} z_{l,\vec{i}} c^\dagger_{\vec{i}}|0\rangle$, the local DOS at site $\vec{i}$ is calculated from $D_{\vec{i}}(E) = \sum_l \delta(E-E_l)|z_{l,\vec{i}}|^2$, which reveals local electronic properties.[49]

We consider that the total energy $E_{\rm tot}$ is obtained by minimizing the energy of the system with respect to all degrees of freedom, including the electronic ones, except for the lattice degrees of freedom. Therefore, $E_{\rm tot}$ is used for calculations of the energy landscape and the Euler simulations, whereas $H_{\rm SSH}$ is used for calculations of electronic properties associated with templates of lattice distortions.

D. Energy landscape for homogeneous states

For the analysis of the energy landscape for homogeneous states, we define the following variables:

$$\tilde{e}_1 \equiv e_1(\vec{k}=0), \quad (6)$$

$$\tilde{e}_2 \equiv e_2(\vec{k}=0), \quad (7)$$

$$\tilde{e}_3 \equiv e_3(\vec{k}=0), \quad (8)$$

$$\tilde{s}_x \equiv s_x[\vec{k}=(\pi,\pi)], \quad (9)$$

$$\tilde{s}_y \equiv s_y[\vec{k}=(\pi,\pi)]. \quad (10)$$

We expect the ground state of $E_{\rm tot}$ to be homogeneous with $\tilde{e}_1$, $\tilde{e}_2$, $\tilde{e}_3$, $\tilde{s}_x$, and $\tilde{s}_y$ distortions only. Therefore, we study the following energy expression, which includes these particular distortions only, to understand the energy landscape for the homogeneous states:

$$E^h_{\rm tot} = E^h_s + E^h_l + E^h_c, \quad (11)$$

$$\frac{E^h_s}{N^2} = \frac{B}{2}\left(\tilde{s}_x^2+\tilde{s}_y^2\right) + \frac{G_1}{4}\left(\tilde{s}_x^4+\tilde{s}_y^4\right) + \frac{G_2}{2}\tilde{s}_x^2\tilde{s}_y^2 + \frac{H_1}{6}\left(\tilde{s}_x^6+\tilde{s}_y^6\right) + \frac{H_2}{6}\tilde{s}_x^2\tilde{s}_y^2\left(\tilde{s}_x^2+\tilde{s}_y^2\right), \quad (12)$$

$$\frac{E^h_l}{N^2} = \frac{A_1}{2}\tilde{e}_1^2 + \frac{A_2}{2}\tilde{e}_2^2 + \frac{A_3}{2}\tilde{e}_3^2, \quad (13)$$

$$\frac{E^h_c}{N^2} = C_3\left(\tilde{s}_x^2-\tilde{s}_y^2\right)\tilde{e}_3. \quad (14)$$

Because $\tilde{e}_1$, $\tilde{e}_2$, $\tilde{e}_3$, $\tilde{s}_x$, and $\tilde{s}_y$ are independent of each other, as explained in Appendix A, we minimize $E^h_{\rm tot}$ with respect to $\tilde{e}_1$, $\tilde{e}_2$, and $\tilde{e}_3$ independently and obtain $\tilde{e}_1=0$, $\tilde{e}_2=0$, $\tilde{e}_3 = -C_3(\tilde{s}_x^2-\tilde{s}_y^2)/A_3$, and the following energy expression in terms of $\tilde{s}_x$ and $\tilde{s}_y$ only:

$$\frac{E^{h,\min}_{\rm tot}}{N^2} = \frac{B}{2}\left(\tilde{s}_x^2+\tilde{s}_y^2\right) + \left(\frac{G_1}{4}-\frac{C_3^2}{2A_3}\right)\left(\tilde{s}_x^4+\tilde{s}_y^4\right) + \left(\frac{G_2}{2}+\frac{C_3^2}{A_3}\right)\tilde{s}_x^2\tilde{s}_y^2 + \frac{H_1}{6}\left(\tilde{s}_x^6+\tilde{s}_y^6\right) + \frac{H_2}{6}\tilde{s}_x^2\tilde{s}_y^2\left(\tilde{s}_x^2+\tilde{s}_y^2\right). \quad (15)$$

We find parameter values for which $E^{h,\min}_{\rm tot}/N^2$ has one local energy minimum state without distortion, $(\tilde{s}_x,\tilde{s}_y)=(0,0)$, and four symmetry-related degenerate global energy minimum states with distortions, $(\tilde{s}_x,\tilde{s}_y)=(\pm s_0,0)$, $(0,\pm s_0)$, where s_0 is the size of the minimum energy s_x or s_y distortion.[50,51] For comparison, we choose two sets of parameter values, one giving a shallow and the other a deep local energy minimum at $(\tilde{s}_x,\tilde{s}_y)=(0,0)$, as shown with a thin blue and a thick red curve, respectively, in Fig. 3, part of which is shown in Ref. 10. In manganites, such a difference in energy landscape can be related to the size of the rare-earth or alkaline-earth metal elements, which is known experimentally to influence the physical properties of manganites.[33] Alternatively, we may consider this a measure of "microstrain."[53] For the parameter values with the deep local energy minimum, the energy difference between local and global minima is about 6 meV per site, similar to the energy difference per Mn ion between metallic and insulating phases of the manganites with phase coexistence.[16]

E. Methods of simulations for inhomogeneous states

To study inhomogeneous states, particularly metastable states, we first minimize $E_{\rm tot}$ analytically with respect to all the independent variables except $s_x(\vec{i})$ and $s_y(\vec{i})$, and we obtain an energy expression $E'_{\rm tot}(s_x,s_y)$. The details of the derivation and the expression for $E'_{\rm tot}(s_x,s_y)$ are provided in Appendix B. The energy landscape of $E'_{\rm tot}(s_x,s_y)$ for inhomogeneous states in $2N^2$-dimensional space is much more complicated than that of homogeneous states in Fig. 3, possibly glasslike,[54,55] because of the effective long-range interactions as a result of the constraints among the distortion modes.

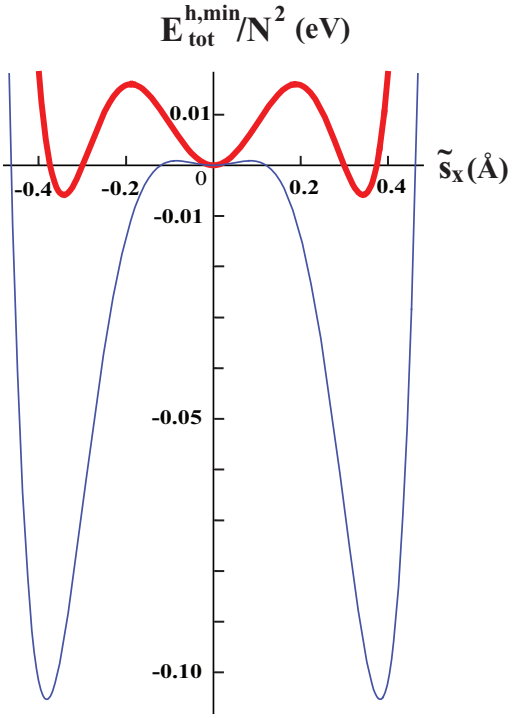

FIG. 3. (Color online) Energy landscape for the homogeneous states. $E_{\rm tot}^{h,\rm min}/N^2$ vs $\tilde{s}_x$ with $\tilde{s}_y = 0$ for the two chosen parameter sets. The parameter values for the deep local energy minimum case, represented by the thick red curve, are $A_1 = 7\,\text{eV/Å}^2$, $A_2 = 4\,\text{eV/Å}^2$, $A_3 = 6$ eV/Å^2, $B = 2$ eV/Å^2, $C_3 = 20$ eV/Å^3, $G_1 = 60$ eV/Å^4, $G_2 = 80\,\text{eV/Å}^4$, $H_1 = 480\,\text{eV/Å}^6$, and $H_2 = 640\,\text{eV/Å}^6$, for which the minimum energy distortions are $s_0 = 0.34$ Å and $|\tilde{e}_3| = 0.39$ Å, and $E_{\rm tot}^{h,\rm min}/N^2$ has a value of -0.0058 eV for the global energy minimum states. The height of the energy barrier between the local and global energy minima is 0.0160 eV, measured from the local energy minimum. These parameter values give rise to an energy difference of about 6 meV per site between distorted and undistorted phases, similar to the energy difference per Mn ion between ferromagnetic undistorted metallic and antiferromagnetic distorted insulating phases of the manganites. The size of the minimum energy distortion s_0 is also of the same order of magnitude as that of the Jahn-Teller distortion observed in manganites.[52] The only different parameter value for the shallow local minimum case, represented by the thin blue curve, is $B = 0.5\,\text{eV/Å}^2$, which gives rise to $s_0 = 0.38$ Å, $|\tilde{e}_3| = 0.49$ Å, the global energy minimum $E_{\rm tot}^{h,\rm min}/N^2$ of -0.1053 eV, and the energy barrier of 0.0009 eV.

In our simulations, we set initial configurations of $s_x(\vec{i})$ and $s_y(\vec{i})$ and relax the lattice according to the Euler method,

$$s_x^{n+1}(\vec{i}) = s_x^n(\vec{i}) - \gamma \left.\frac{\partial E'_{\rm tot}(s_x,s_y)}{\partial s_x(\vec{i})}\right|_{s_x^n,s_y^n}, \quad (16)$$

$$s_y^{n+1}(\vec{i}) = s_y^n(\vec{i}) - \gamma \left.\frac{\partial E'_{\rm tot}(s_x,s_y)}{\partial s_y(\vec{i})}\right|_{s_x^n,s_y^n}, \quad (17)$$

where the superscript n or $n+1$ represents the number of Euler steps taken from the initial configuration, and γ controls the size of the Euler step. Expressions for $\partial E'_{\rm tot}(s_x,s_y)/\partial s_x(\vec{i})$ and $\partial E'_{\rm tot}(s_x,s_y)/\partial s_y(\vec{i})$ are provided in Appendix C. We run the simulations until $E'_{\rm tot}(s_x,s_y)$ reaches equilibrium.

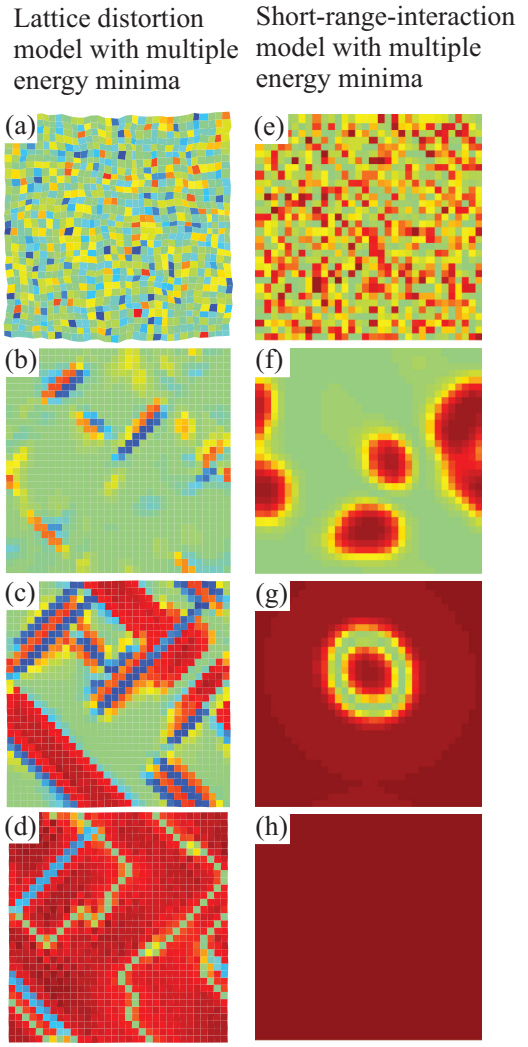

FIG. 4. (Color online) Left column: Simulation for the relaxation of lattice distortions for a 32×32 lattice. The energy landscape with a shallow local minimum, which is represented by the thin blue curve in Fig. 3, is considered here. The vertices correspond to the displaced positions of atoms. The color represents $p_3 = s_x^2 - s_y^2$, with green corresponding to zero, and red and blue corresponding to $\pm s_0^2$, except $\pm(2.6s_0)^2$ for panel (a). Right column: Simulation of the relaxation for a model with a short-range interaction only, for comparison with the lattice distortion model on the left. The variable $p = M^2$ is plotted on a 32×32 lattice with a periodic boundary condition. Red represents $p = 28.6M_0^2$ for (e) and $p = M_0^2$ for (f)–(h), and green represents $p = 0$.

F. Initial conditions and results of the simulations for inhomogeneous states

Figures 4(a)–4(d) show the results of simulations carried out on a 32×32 lattice for the energy landscape with a shallow local minimum, shown in the thin blue curve in Fig. 3 for homogeneous states. The color of each plaquette represents $p_3(\vec{i}) \equiv s_x(\vec{i})^2 - s_y(\vec{i})^2$, and the vertices of plaquettes represent the locations of displaced atoms. Through the coupling between p_3 and e_3 in E_c, positive and negative values of p_3 are usually accompanied by an e_3 distortion elongated along the y and x direction, respectively. Most plaquettes with p_3 close to zero have little distortion. Starting from an initial

configuration of $s_x(\vec{i})$ and $s_y(\vec{i})$ randomly chosen between $-2s_0$ and $2s_0$ as shown in Fig. 4(a), the system is relaxed through the Euler method with $\gamma = 0.0015$ Å^2/eV. Figures 4(b)–4(d) correspond to the configurations at the Euler step, $n = 1000$ and 4000, and the stable configuration at $n = 100\,000$, respectively.[56] Following the energy gradient from a random initial configuration, the simulation approximately represents a rapid quenching of the system from a very high temperature to 0 K.

For comparison, we study a system with a similar energy expression,

$$E_M = \sum_{\vec{i}} \frac{W}{2} M_{\vec{i}}^2 + \frac{X}{4} M_{\vec{i}}^4 + \frac{Y}{6} M_{\vec{i}}^6 + \frac{Z}{2}\{[M_{\vec{i}+(1,0)} - M_{\vec{i}}]^2 + [M_{\vec{i}+(0,1)} - M_{\vec{i}}]^2\}, \quad (18)$$

but without constraint or long-range interaction between variables $M_{\vec{i}}$. The last term becomes $Z(\nabla M)^2/2$, the familiar Ginzburg-Landau gradient term, in the continuum limit. Parameter values are chosen[57] so that the energy landscape is similar to the lattice distortion model and the uniform ground state for E_M is $M_{\vec{i}} = \pm M_0 = \pm 0.38$, identical to s_0 in Å. Figures 4(e)–4(h) show the results of a simulation on a 32×32 lattice, in which $p = M^2$, analogous to p_3 for the lattice distortion model, is shown. The initial configuration of $M_{\vec{i}}$, shown in Fig. 4(e), is chosen randomly between $-5.3M_0$ and $5.3M_0$, and is relaxed according to the Euler method.[58] Both systems in Fig. 4 show nucleation and growth of the low-energy phases, as expected for the first-order-like energy landscape. However, comparison between the left and right columns reveals distinct features present only in the lattice distortion model.

First, the nucleation droplets in Fig. 4(b) are highly anisotropic, in contrast with those in Fig. 4(f). Second, distortions separated by a relatively large distance along the diagonal direction interact with each other, grow toward each other, and merge through the long-range interaction, as seen for the yellow and red band along the 135 degree orientation in Figs. 4(b) and 4(c). Such characteristics of the long-range interaction cannot be identified in Figs. 4(f) and 4(g). Third, the nucleation occurs via pairs of distortions with different orientations to minimize the interface energy between the distorted region and the undistorted background, as shown in Fig. 4(b). Such features are absent in the panels of the right column in Fig. 4, where the interaction is purely short-ranged. Recent x-ray scattering experiments have revealed the presence of short-range anisotropic precursor correlations in the orthorhombic phase of manganites at high temperatures, which disappear in the rhombohedral phase.[5] Such a feature has a similarity with the anisotropic droplets observed in our simulations for the lattice distortion model.

For the deep local-energy-minimum case described by the thick red curve in Fig. 3, simulations of rapid quenching using the Euler method for a 64×64 lattice do not create the nucleation of the low-energy phase. Instead, we obtain an undistorted homogeneous state as the final state, which is an indication of strong metastability due to a higher-energy barrier between the distorted and undistorted states. In crystals, we expect that line or planar defects as well as thermal

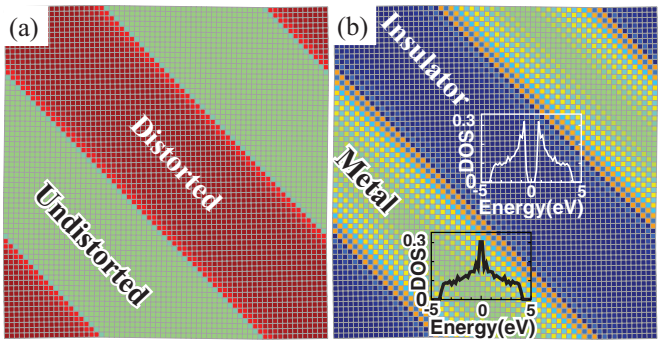

FIG. 5. (Color online) (a) Stable configuration of distorted and undistorted domains for a 64×64 lattice for the energy landscape with a deep local minimum, shown by the thick red curve in Fig. 3. The color represents p_3 with red and green for s_0^2 and 0, respectively. (b) Map of the local electron DOS calculated at $E = 0$ for the distortions in (a). Red, green, and blue correspond to 0.6, 0.3, and 0 state per site per eV, respectively. The local electron DOS per site per eV calculated at the center of the undistorted and the distorted regions is shown over the corresponding domains.

fluctuations would assist the nucleation. Simulations of such processes require more computational resources. Therefore, we start from predesigned initial states and relax the lattice to obtain stable coexistence of distorted and undistorted domains. An initial state is chosen according to

$$s_x(\vec{i}) = s_0(-1)^{i_x+i_y}\left\{\cos\left[\frac{2\pi(i_x+i_y-4)}{N}\right] + \frac{1}{2}\right\}, \quad (19)$$

$$s_y(\vec{i}) = 0, \quad (20)$$

with $N = 64$, and it is relaxed with $\gamma = 0.0002$ Å^2/eV. As a result, we obtain a stable configuration shown in Fig. 5(a). We find stable coexistence of large undistorted [green region in Fig. 5(a)] and distorted [red region in Fig. 5(a)] domains, unlike the shallow-local-minimum case. The size of the domain is determined only by the initial condition, and therefore it can be as large as several micrometers, consistent with experimental results for manganites.

For comparison, we again carry out simulations for the system with a short-range interaction only, described by E_M in Eq. (18) with a similar energy landscape and a predesigned initial state,

$$M_{\vec{i}} = M_0\left\{\cos\left[\frac{2\pi(i_x+i_y)}{N}\right] + c_s\right\}. \quad (21)$$

For $c_s = 0.5$, $\gamma = 0.0002$, and $N = 64$, we find that the final stable configuration is a uniform ground state, rather than a state with domains. For $c_s = 0$, $\gamma = 0.0002$, and $N = 128$, we find only a line of atoms, rather than a domain, with M close to zero between regions with $M = M_0$ and $M = -M_0$. This comparison shows that the strain-strain long-range interaction indeed plays an essential role for the coexistence of the distorted and undistorted phases.

To demonstrate electronic inhomogeneity associated with the structural inhomogeneity, we calculate the electronic properties for the template of the lattice distortions in Fig. 5(a). We use the SSH Hamiltonian in Eq. (5) with $t_0 = 1$ eV and $\alpha = 1$ Å^{-1}, similar to the electron hopping amplitude and the

Jahn-Teller coupling constant for manganites, which results in a gap of about 1 eV for the distorted phase, similar to the Jahn-Teller gap for the manganites. Typical local electron DOSs within the undistorted and distorted regions are shown over the corresponding domains in Fig. 5(b). The local DOS is symmetric about the energy $E = 0$, and a gap opens near $E = 0$ in distorted regions, as obtained in Ref. 44. Therefore, the distorted and undistorted regions have insulating and metallic electron DOSs, respectively, at half-filling without any spatial charge inhomogeneity. The map of the local electron DOS at $E = 0$ is shown in the background of Fig. 5(b).

The possible inhomogeneity in the local DOS without any charge inhomogeneity in our model is in contrast with other explanations for the inhomogeneity based on electronic phase separation.[6] Our results also indicate that chemical inhomogeneity is not a necessary condition to have a large-scale coexistence of metallic and insulating domains, which is in contrast to other theories.[7] Although lattice defects or segregation of dopants could play a role in nucleation, the stability of the metal-insulator coexistence relies on intrinsic energy landscapes, which explains why external perturbations such as focused x rays,[35] light,[59] or electron beams alter metallic and insulating domains in manganites.

III. STABILITY OF PHASE COEXISTENCE

A. Stability against uniform domain wall motions

Unlike twin boundaries between two domains of the *same* energy, the metal-insulator boundaries in Fig. 5 split two phases with *different* energies. Thus, it could usually be anticipated that the metal-insulator boundaries would advance into the higher-energy metallic phase and lower the total energy of the system, and the stable metal-insulator coexistence in Fig. 5 is surprising. Therefore, in this section, we examine the stability of the metal-insulator coexistence against various kinds of perturbations and find the mechanism for the stability. First, we examine the energy barrier blocking a uniform shift of the metal-insulator boundaries. Red dots connected by the lowest line in Fig. 6 show $s_x(i_x,i_y)(-1)^{i_x+i_y}$ versus i_x for $i_y = 1$ near the boundary between the undistorted (i.e., $i_x \leqslant 51$) and distorted (i.e., $i_x \geqslant 52$) phases for the configuration in Fig. 5(a). To find the energy barrier against uniform domain wall shift, we increase the value of $s_x(i_x,i_y)(-1)^{i_x+i_y}$ at the sites immediately adjacent to the domain boundary, that is, at $i_x = 51 - i_s$, $i_y = 1 + i_s$ with integer i_s's, in eight steps from near zero to the full distortion close to s_0. At each step, we minimize the total energy with respect to the distortions at all other sites using the Euler method. This gives rise to distortion profiles shown by dots of different colors in Fig. 6. The two-dimensional configurations for the red, green, and purple dots in Fig. 6 are also shown in Figs. 7(a)–7(c), respectively, where the colors represent s_x. The results show that $s_x(i_x,i_y)(-1)^{i_x+i_y}$ at (51,1), (50,1), and similar sites adjacent to the domain boundary, grow together, compensating for s_x distortions with opposite signs at the two neighboring sites, and the domain boundary advances by two interatomic distances.

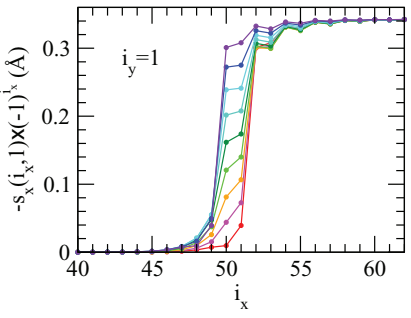

FIG. 6. (Color online) The red dots represent the profiles of $s_x(i_x,i_y)(-1)^{i_x+i_y}$ with $i_y = 1$ near the domain boundary in Fig. 5(a). Dots of other colors show how this profile changes as the domain boundary shifts uniformly by two interatomic distances.

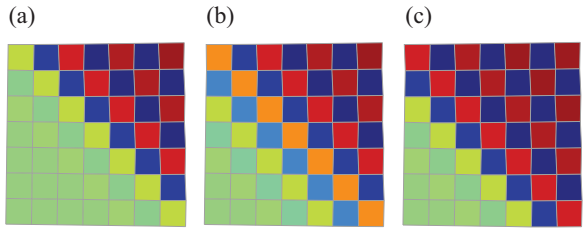

FIG. 7. (Color online) Configurations of lattice distortions near the domain boundary, as the boundary moves by two interatomic distances. The color scheme is different from Figs. 4 and 5(a). Here, the colors represent the s_x mode, with red, green, and blue corresponding to s_0, 0, and $-s_0$, respectively. Parts (a)–(c) correspond to the profiles represented by red, green, and purple dots in Fig. 6.

For a further quantitative analysis of the energy barrier, we define the effective location of the domain boundary, $d_{\rm db}$, according to

$$d_{\rm db} = 2 \times \frac{s_x^* - 0.040\ \text{Å}}{0.308\ \text{Å} - 0.040\ \text{Å}}, \tag{22}$$

where s_x^* represents the value of $s_x(i_x,i_y)(-1)^{i_x+i_y}$ chosen at $i_x = 51$ in Fig. 6, and 0.040 and 0.308 Å are the values of s_x^* before and after the domain wall moves by two interatomic distances. Minimized total energy $E'_{\rm tot}$ is plotted in Fig. 8 for $0 \leqslant d_{\rm db} \leqslant 2$, which shows an energy barrier, an example of the Peierls-Nabarro barrier.[25] We compare three energies, $E_1 = -2.946$ eV, $E_2 = -1.668$ eV, and $E_3 = -3.693$ eV for

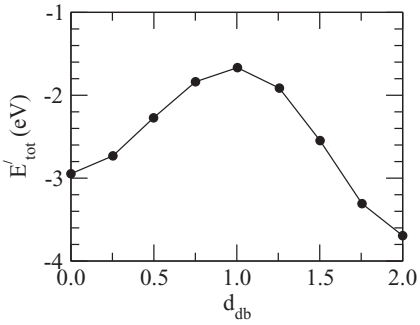

FIG. 8. Total energy $E'_{\rm tot}$ for the 64 × 64 system, given by Eq. (B26), vs the location of the domain boundary defined by Eq. (22), as the boundary moves by two interatomic distances. Each point is found from each corresponding curve in Fig. 6. The configurations in Figs. 7(a)–7(c) correspond to $d_{\rm db} = 0.0$, 1.0, and 2.0, respectively.

$d_{\rm db} = 0.0$, 1.0, and 2.0, which correspond to the configurations shown in Figs. 7(a)–7(c), respectively. Most changes in the distortion occur in the 64×2 plaquettes near the domain boundary, as shown in Figs. 6 and 7. Therefore, the energy difference between the two stable domain configurations for $d_{\rm db} = 0.0$ and 2.0 is $(E_1 - E_3)/128 = 0.0058$ eV per site, which agrees with the energy difference per site between the undistorted and distorted uniform phases in Fig. 3. The energy barrier normalized for 64×2 plaquettes, that is, $(E_2 - E_1)/128$, is 0.0100 eV, which is a little lower than the height of the energy barrier per site, $\Delta E_{\rm per\ site} = 0.0160$ eV, between the local and global energy minima in Fig. 3.

From this analysis, we obtain the energy barrier against the uniform shift of the domain wall of the order of $2\Delta E_{\rm per\ site}$ multiplied by the domain wall length in the unit of the interatomic distance, which would be a macroscopic energy barrier for the domain walls of micron length scale. Discreteness of the lattice in our model is essential for the Peierls-Nabarro energy barrier, and traditional continuum models such as the phase field model would not support the stable metal-insulator coexistence in Fig. 5 in the absence of defects.

B. Stability against nonuniform domain wall modifications

The importance of the long-range interaction between strain fields is more evident for the stability against nonuniform modifications of the metal-insulator boundaries. As an example, we convert a patch of the undistorted region in a configuration similar to Fig. 5(a) into a distorted state initially, and we relax the whole lattice according to the Euler method. The initial, two intermediate, and final configurations are displayed in Fig. 9. The results show that the distortion in the converted region disappears initially except for two atomic layers [Fig. 9(c)], the width of which shrinks by further relaxation, restoring the original configuration [Fig. 9(d)]. The simulation demonstrates the stability of the metal-insulator coexistence against nonuniform modifications of the interface. We emphasize here that a similar simulation with the continuum elastic theory starting from a configuration like Fig. 9(a) would further relax the configuration in Fig. 9(d) into a homogeneous state with the low-energy phase, because of the absence of the Peierls-Nabarro energy barrier. Therefore, the long-range anisotropic elastic interaction is not enough, but the atomic discreteness also plays an essential role in the absence of defects for the stability of the metal-insulator coexistence.

To gain further insight into the role of lattice compatibility, we examine other modes and energy distribution. Figures 10(a)–10(c) show the modes, e_1, e_2, and e_3 for the s_x distortions in Fig. 9(b). The strain fields tend to spread into the domains from the domain boundary. In particular, the e_3 field inside the converted patch in Fig. 10(c) cannot reach $-C_3 s_0^2/A_3$, the full distortion of e_3 inside the domain, due to the strain compatibility. The map of $E_{\rm tot}(\vec{i})$, the sum of the terms with the site index $\vec{i}$ in Eqs. (2)–(4), is displayed in Fig. 10(d), which shows that the energy cost for creating the distorted patch is not confined near the interface, but is distributed over the whole converted patch, as observed in the continuum phase field model.[23,24] This is different from

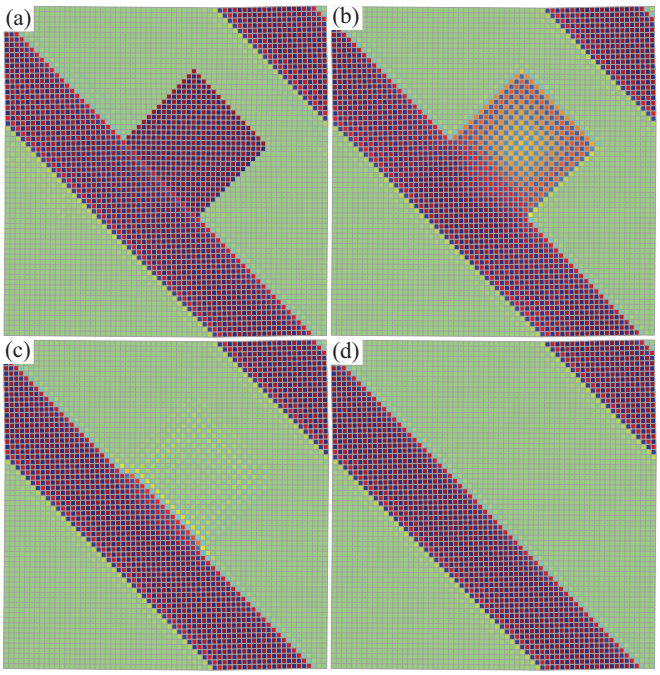

FIG. 9. (Color online) Simulation of the domain wall stability against a small nonuniform modification of the domain boundary for the configuration similar to Fig. 5(a). The color scheme is identical to Fig. 7. Part (a) represents the initial perturbed configuration. Parts (b) and (c) show intermediate configurations. Part (d) represents the final stable configuration, which is identical to the original configuration before the perturbation.

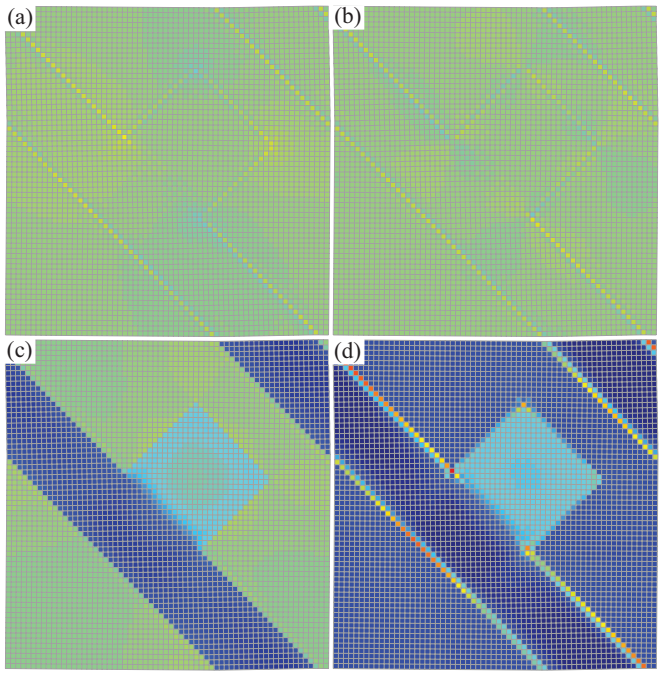

FIG. 10. (Color online) Modes and energy distribution for the configuration shown in Fig. 9(b). Colors in (a)–(c) show $e_1(\vec{i})$, $e_2(\vec{i})$, and $e_3(\vec{i})$ with red and blue corresponding to ± 0.45 Å and green to zero. Colors in (d) show $E_{\rm tot}(\vec{i})$, which is the sum of the terms with the site index $\vec{i}$ in Eqs. (2)–(4), with red and blue corresponding to 0.06 and -0.006 eV, respectively. Typical values of $e_3(\vec{i})$ and $E_{\rm tot}(\vec{i})$ inside the converted patch are -0.08 and 0.02 eV, respectively.

systems with short-range interactions only, for which the energy cost would be confined near the domain walls within the range of the interaction. This difference shows that the lattice constraint, leading to the effective long-range interaction, plays an important role in the stability of the metal-insulator phase coexistence in manganites against nonuniform modifications of metal-insulator boundaries. Similarly, we find that if we convert a patch of the distorted region of a similar size into the undistorted state, the system relaxes back to the original configuration.

However, the above results do not mean that it is impossible to change the phase of a region. For example, as shown in Fig. 11, if we convert a large enough patch [Fig. 11(a)], even though the distortions in most of the converted region disappear initially, the distortions in two layers next to the original domain boundary remain [Fig. 11(b)], the width of which expands [Fig. 11(c)]. Eventually, the distorted domain grows by two atomic layers [Fig. 11(d)]. The different relaxation behavior between the configurations in Figs. 9(c) and 11(b) shows that the growth of the low-energy phase involves simultaneous changes in distortions of a significant number of unit cells next to the interface. Such a collective change of distortions would require overcoming a mesoscopic energy barrier, which would involve a time scale much longer than the atomic time scale. Slow growth of the low-energy phase has been observed in a number of experiments for manganites. For example, Ref. 21 reports a time scale of the order of 10 min for the growth of the low-energy phase. A rough order-of-magnitude estimate of the energy barrier ΔE can be made by assuming an activated thermal process so that the relaxation time is given by $\tau = \tau_0 \exp(\Delta E / k_B T)$, where τ_0 represents the intrinsic time scale for ion motion, k_B is the Boltzmann constant, and T is the temperature. With $\tau \sim 10^3$ s, $\tau_0 \sim 10^{-13}$ s, and $k_B T \sim 10$ meV, we obtain ΔE of the order of 1 eV. If we consider the typical energy scale for the distortion of the unit cell to be 1–10 meV, this energy barrier corresponds to about 100–1000 unit cell distortions within the layer next to the two-dimensional interface, consistent with our simulations. A similar growth of the undistorted metallic region occurs if we convert a large enough distorted region into the undistorted state, as shown in Fig. 12. The result is reminiscent of experiments in which the volume fraction of the undistorted phase is increased by external perturbations such as x rays or light.[35,59]

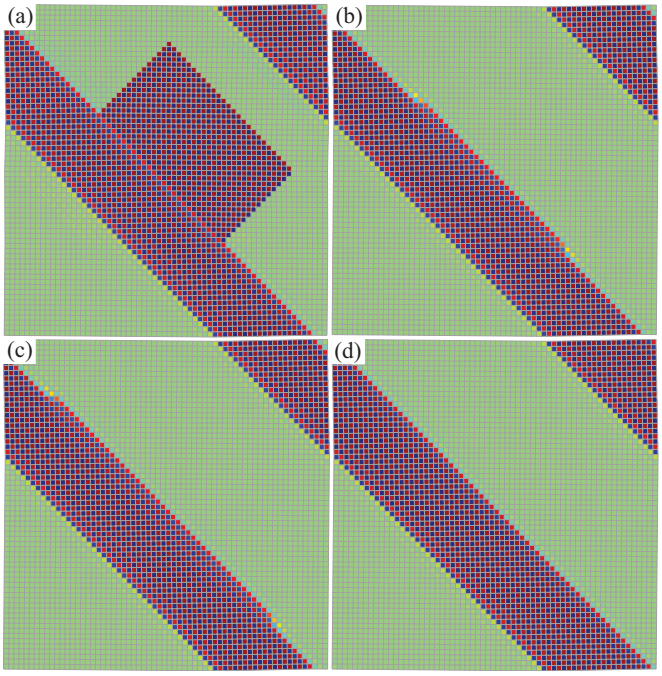

FIG. 11. (Color online) Simulation of the growth of the low-energy insulating phase by a nonuniform modification of the domain boundary, converting a large enough undistorted patch into a distorted state, for the configuration similar to Fig. 5(a). The color scheme is identical to Fig. 7. An initial configuration is shown in (a). Parts (b) and (c) show intermediate configurations. Part (d) represents the final stable configuration, which shows that the distorted region has expanded by two atomic layers.

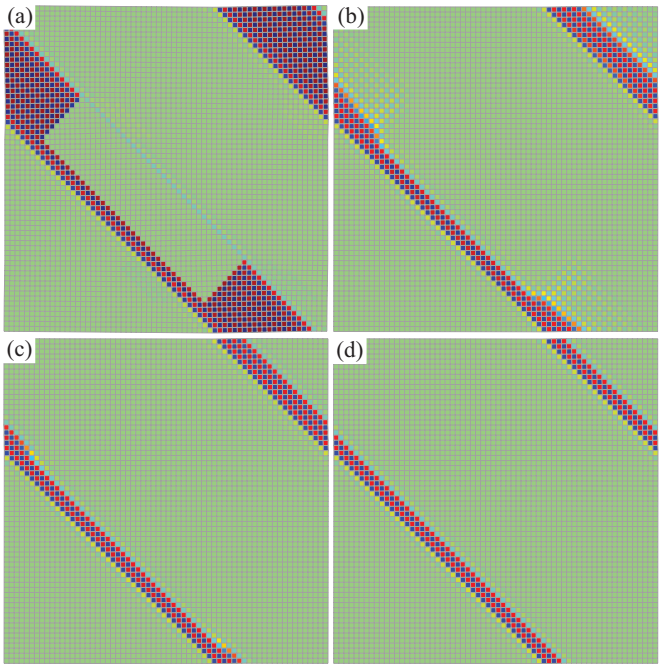

FIG. 12. (Color online) Simulation of the growth of the high-energy metallic phase by a nonuniform modification of the domain boundary, converting a large enough distorted patch into an undistorted state, for a configuration similar to Fig. 5(a). The color scheme is identical to Fig. 7. An initial configuration is shown in (a). Parts (b) and (c) show intermediate configurations. Part (d) represents the final stable configuration.

The results in this subsection demonstrate the important role played by the long-range anisotropic strain-strain interaction for the stability of the metal-insulator phase coexistence against nonuniform perturbations of the interface.

IV. SUMMARY

We have discussed various aspects of a model for the strain-induced phase coexistence observed in perovskite manganites. A square lattice and associated atomic-scale distortion modes were used to construct an energy expression with local and global energy minimum states, which captures features of

manganites essential for phase coexistence: a metallic local-energy-minimum state without lattice distortions and an insulating global-energy-minimum state with short wavelength and uniform lattice distortions. Expressions for modes, constraint equations, energies, and energy gradients have been presented. Our simulations for an energy landscape with a shallow local-energy-minimum state revealed nucleation with anisotropic correlations upon rapid quenching. Our simulations for an energy landscape with a deep local-energy-minimum state showed stable coexistence of undistorted metallic and distorted insulating domains. Further, we studied the stability of such metal-insulator coexistence against various perturbations. We found that domain configurations are stable against uniform shift of the boundary due to the discreteness of the lattice and the intrinsic energy barrier between local- and global-energy-minimum states. For nonuniform modifications of metal-insulator boundaries, the long-range interaction between strain fields gave rise to the domain wall energy distributed over the whole modified area for our two-dimensional model (or volume for three-dimensional systems), rather than the region confined near the domain wall, providing extra stability in addition to the Peierls-Nabarro energy barrier to the phase coexistence. To provide a comparison, we carried out simulations for a system with a short-range interaction only, which showed no anisotropic nucleation or stable coexistence of local and global energy minimum phases. The results demonstrate that the long-range interaction between stain fields, complex energy landscapes, and the Peierls-Nabarro energy barrier play an important role in metal-insulator coexistence in perovskite manganites.[60]

ACKNOWLEDGMENTS

We thank Avadh Saxena and Yoonseok Lee for discussions. This work has been supported by US DOE/LANL Award No. DE-AC52-06NA25396/170590-1 (T.F.S. and K.H.A.) and by US DOE LANL LDRD (T.L. and A.R.B.).

APPENDIX A: DEFINITION OF MODES, THEIR CONSTRAIN EQUATIONS, AND RELATIONS IN RECIPROCAL SPACE

Displacement of atoms in a periodic structure can be described using two components. One is the component that changes monotonically as the site indices shift along a direction. This component, represented by a superscript "nF" below, cannot be Fourier-transformed and corresponds to the uniform distortion of the lattice. The rest of the displacement, represented by a superscript "F" below, can be Fourier-transformed and is subject to periodic boundary conditions. Therefore, we express the displacements as follows:

$$u_{\vec{i}}^{x} = u_{\vec{i}}^{x,\mathrm{nF}} + u_{\vec{i}}^{x,\mathrm{F}}, \tag{A1}$$

$$u_{\vec{i}}^{y} = u_{\vec{i}}^{y,\mathrm{nF}} + u_{\vec{i}}^{y,\mathrm{F}}, \tag{A2}$$

where

$$u_{\vec{i}}^{x,\mathrm{nF}} = \varepsilon_0^{xx} i_x + \varepsilon_0^{xy} i_y, \tag{A3}$$

$$u_{\vec{i}}^{y,\mathrm{nF}} = \varepsilon_0^{xy} i_x + \varepsilon_0^{yy} i_y, \tag{A4}$$

$$u_{\vec{i}}^{x,\mathrm{F}} = \sum_{\vec{k}} u_{\vec{k}}^{x} e^{i\vec{k}\cdot\vec{i}}, \tag{A5}$$

$$u_{\vec{i}}^{y,\mathrm{F}} = \sum_{\vec{k}} u_{\vec{k}}^{y} e^{i\vec{k}\cdot\vec{i}}, \tag{A6}$$

and ε_0^{xx}, ε_0^{xy}, and ε_0^{yy} are strain tensors from the continuum theory of elasticity.

Periodic boundary conditions result in $k_x = \frac{2\pi n_x}{N}$ and $k_y = \frac{2\pi n_y}{N}$, where $n_x = -N/2-1, \ldots, N/2$ and $n_y = -N/2-1, \ldots, N/2$. For $u_{\vec{i}}^{x,\mathrm{nF}}$ and $u_{\vec{i}}^{y,\mathrm{nF}}$, the rigid rotation of the whole system is excluded, since it is irrelevant to the potential energy change. Similarly, the $\vec{k}=0$ components of $u_{\vec{i}}^{x,\mathrm{F}}$ and $u_{\vec{i}}^{y,\mathrm{F}}$ correspond to the rigid translations of the whole system, which are set to zero.

For the square lattice, we define the symmetry modes shown in Fig. 2 as follows:

$$e_1(\vec{i}) = \frac{1}{2\sqrt{2}}\big(-u_{\vec{i}}^{x} - u_{\vec{i}}^{y} + u_{\vec{i}+10}^{x} - u_{\vec{i}+10}^{y} - u_{\vec{i}+01}^{x} + u_{\vec{i}+01}^{y} + u_{\vec{i}+11}^{x} + u_{\vec{i}+11}^{y}\big), \tag{A7}$$

$$e_2(\vec{i}) = \frac{1}{2\sqrt{2}}\big(-u_{\vec{i}}^{x} - u_{\vec{i}}^{y} - u_{\vec{i}+10}^{x} + u_{\vec{i}+10}^{y} + u_{\vec{i}+01}^{x} - u_{\vec{i}+01}^{y} + u_{\vec{i}+11}^{x} + u_{\vec{i}+11}^{y}\big), \tag{A8}$$

$$e_3(\vec{i}) = \frac{1}{2\sqrt{2}}\big(-u_{\vec{i}}^{x} + u_{\vec{i}}^{y} + u_{\vec{i}+10}^{x} + u_{\vec{i}+10}^{y} - u_{\vec{i}+01}^{x} - u_{\vec{i}+01}^{y} + u_{\vec{i}+11}^{x} - u_{\vec{i}+11}^{y}\big), \tag{A9}$$

$$s_x(\vec{i}) = \frac{1}{2}\big(u_{\vec{i}}^{x} - u_{\vec{i}+10}^{x} - u_{\vec{i}+01}^{x} + u_{\vec{i}+11}^{x}\big), \tag{A10}$$

$$s_y(\vec{i}) = \frac{1}{2}\big(u_{\vec{i}}^{y} - u_{\vec{i}+10}^{y} - u_{\vec{i}+01}^{y} + u_{\vec{i}+11}^{y}\big). \tag{A11}$$

These modes are fully subject to the periodic boundary conditions. Thus, they can be Fourier-transformed, for example, according to

$$e_1(\vec{i}) = \sum_{\vec{k}} e_1(\vec{k}) e^{i\vec{k}\cdot\vec{i}}. \tag{A12}$$

From the definitions, we find

$$e_1(\vec{k}=0) = \frac{\varepsilon_0^{xx} + \varepsilon_0^{yy}}{\sqrt{2}} = \tilde{e}_1, \tag{A13}$$

$$e_2(\vec{k}=0) = \frac{\varepsilon_0^{xy}}{\sqrt{2}} = \tilde{e}_2, \tag{A14}$$

$$e_3(\vec{k}=0) = \frac{\varepsilon_0^{xx} - \varepsilon_0^{yy}}{\sqrt{2}} = \tilde{e}_3, \tag{A15}$$

$$s_x(\vec{k}=0) = 0, \tag{A16}$$

$$s_y(\vec{k}=0) = 0, \tag{A17}$$

$$e_1(\vec{k}\neq 0) = \frac{1}{2\sqrt{2}}\big[-(1-e^{ik_x})(1+e^{ik_y})u_{\vec{k}}^{x} - (1+e^{ik_x})(1-e^{ik_y})u_{\vec{k}}^{y}\big], \tag{A18}$$

$$e_2(\vec{k}\neq 0)=\frac{1}{2\sqrt{2}}\big[-(1+e^{ik_x})(1-e^{ik_y})u^x_{\vec{k}} - (1-e^{ik_x})(1+e^{ik_y})u^y_{\vec{k}}\big], \quad \text{(A19)}$$

$$e_3(\vec{k}\neq 0)=\frac{1}{2\sqrt{2}}\big[-(1-e^{ik_x})(1+e^{ik_y})u^x_{\vec{k}} + (1+e^{ik_x})(1-e^{ik_y})u^y_{\vec{k}}\big], \quad \text{(A20)}$$

$$s_x(\vec{k}\neq 0)=\frac{1}{2}(1-e^{ik_x})(1-e^{ik_y})u^x_{\vec{k}}, \quad \text{(A21)}$$

$$s_y(\vec{k}\neq 0)=\frac{1}{2}(1-e^{ik_x})(1-e^{ik_y})u^y_{\vec{k}}. \quad \text{(A22)}$$

The five variables are related by three constraint equations, because only two physically independent displacement variables exist for each site.[39] These constraint equations are found from the relations between the symmetry modes and the displacement variables in reciprocal space. For $k_x\neq 0$ and $k_y\neq 0$, we invert the linear relations between $[s_x(\vec{k}), s_y(\vec{k})]$ and $[u^x_{\vec{k}}, u^y_{\vec{k}}]$ in Eqs. (A21) and (A22) and replace them in the expressions with other modes in Eqs. (A18)–(A20). This leads to

$$\sin\frac{k_x}{2}\cos\frac{k_y}{2}s_x(\vec{k})+\cos\frac{k_x}{2}\sin\frac{k_y}{2}s_y(\vec{k}) - \sqrt{2}i\sin\frac{k_x}{2}\sin\frac{k_y}{2}e_1(\vec{k})=0, \quad \text{(A23)}$$

$$\cos\frac{k_x}{2}\sin\frac{k_y}{2}s_x(\vec{k})+\sin\frac{k_x}{2}\cos\frac{k_y}{2}s_y(\vec{k}) - \sqrt{2}i\sin\frac{k_x}{2}\sin\frac{k_y}{2}e_2(\vec{k})=0, \quad \text{(A24)}$$

$$\sin\frac{k_x}{2}\cos\frac{k_y}{2}s_x(\vec{k})-\cos\frac{k_x}{2}\sin\frac{k_y}{2}s_y(\vec{k}) - \sqrt{2}i\sin\frac{k_x}{2}\sin\frac{k_y}{2}e_3(\vec{k})=0. \quad \text{(A25)}$$

These constraint equations indicate that $e_1(\pi,\pi)$, $e_2(\pi,\pi)$, and $e_3(\pi,\pi)$ vanish and $\tilde{s}_x\equiv s_x(\pi,\pi)$ and $\tilde{s}_y\equiv s_y(\pi,\pi)$ are independent variables. Constraint equations for $k_x=0$ or $k_y=0$ should be considered separately from Eqs. (A23)–(A25). Equations (A13)–(A17) show that $e_1(\vec{k}=0)$, $e_2(\vec{k}=0)$, and $e_3(\vec{k}=0)$ are independent of each other, and $s_x(\vec{k}=0)$ and $s_y(\vec{k}=0)$ vanish. For $k_x=0$ and $k_y\neq 0$, Eqs. (A18)–(A22) show that $e_1(\vec{k})=-e_3(\vec{k})$ and $e_2(\vec{k})$ are independent variables, and $s_x(\vec{k})=s_y(\vec{k})=0$. Similarly, for $k_x\neq 0$ and $k_y=0$, $e_1(\vec{k})=e_3(\vec{k})$ and $e_2(\vec{k})$ are independent variables, and $s_x(\vec{k})=s_y(\vec{k})=0$.

To describe lattice distortions in our simulations, we primarily use the variables $s_x(\vec{i})$ and $s_y(\vec{i})$. These variables can be assigned arbitrarily except that they should satisfy $s_x(\vec{k})=s_y(\vec{k})=0$ if $k_x=0$ or $k_y=0$, as required by Eqs. (A16), (A17), (A21), and (A22). In our numerical simulations, we implement this condition by subtracting unphysical components with $k_x=0$ or $k_y=0$ from $s_x(\vec{i})$ and $s_y(\vec{i})$, each time we initialize or change $s_x(\vec{i})$ and $s_y(\vec{i})$. However, $s_x(\vec{i})$ and $s_y(\vec{i})$ do not uniquely determine lattice distortions, because of the singular relation between $[s_x(\vec{k}), s_y(\vec{k})]$ and $[u^x_{\vec{k}}, u^y_{\vec{k}}]$ in Eqs. (A21) and (A22). As seen above, $e_1(\vec{k}=0)$, $e_2(\vec{k}=0)$, $e_3(\vec{k}=0)$, $e_1(k_x=0,k_y\neq 0)=-e_3(k_x=0,k_y\neq 0)$, $e_2(k_x=0,k_y\neq 0)$, $e_1(k_x\neq 0,k_y=0)=e_3(k_x\neq 0,k_y=0)$, and $e_2(k_x\neq 0,k_y=0)$ should be specified, in addition to $s_x(\vec{i})$ and $s_y(\vec{i})$, for the complete description of lattice distortions.

Displacement variables $u^x_{\vec{i}}$ and $u^y_{\vec{i}}$ are calculated from these modes. For the nonperiodic parts of displacements, $u^{x,\mathrm{nF}}_{\vec{i}}$ and $u^{y,\mathrm{nF}}_{\vec{i}}$ in Eqs. (A3) and (A4), we use Eqs. (6)–(8) to obtain

$$u^{x,\mathrm{nF}}_{\vec{i}}=\frac{e_1(\vec{k}=0)+e_3(\vec{k}=0)}{\sqrt{2}}i_x+\sqrt{2}e_2(\vec{k}=0)i_y, \quad \text{(A26)}$$

$$u^{y,\mathrm{nF}}_{\vec{i}}=\sqrt{2}e_2(\vec{k}=0)i_x+\frac{e_1(\vec{k}=0)-e_3(\vec{k}=0)}{\sqrt{2}}i_y. \quad \text{(A27)}$$

We find the periodic parts of the displacement, $u^{x,\mathrm{F}}_{\vec{i}}$ and $u^{y,\mathrm{F}}_{\vec{i}}$, through the Fourier transformation of $u^x_{\vec{k}}$ and $u^y_{\vec{k}}$, which are obtained by inverting two nonsingular equations among Eqs. (A18)–(A22). Therefore, if $k_x\neq 0$ and $k_y\neq 0$, we invert Eqs. (A21) and (A22) to obtain

$$u^x_{k_x\neq 0,k_y\neq 0}=\frac{2}{(1-e^{ik_x})(1-e^{ik_y})}s_x(\vec{k}), \quad \text{(A28)}$$

$$u^y_{k_x\neq 0,k_y\neq 0}=\frac{2}{(1-e^{ik_x})(1-e^{ik_y})}s_y(\vec{k}). \quad \text{(A29)}$$

If $k_x\neq 0$ and $k_y=0$, Eqs. (A18) and (A19) lead to

$$u^x_{k_x\neq 0,k_y=0}=-\frac{\sqrt{2}}{1-e^{ik_x}}e_1(\vec{k}), \quad \text{(A30)}$$

$$u^y_{k_x\neq 0,k_y=0}=-\frac{\sqrt{2}}{1-e^{ik_x}}e_2(\vec{k}). \quad \text{(A31)}$$

Similarly, if $k_x=0$ and $k_y\neq 0$, we obtain

$$u^x_{k_x=0,k_y\neq 0}=\frac{\sqrt{2}}{1-e^{ik_y}}e_2(\vec{k}), \quad \text{(A32)}$$

$$u^y_{k_x=0,k_y\neq 0}=\frac{\sqrt{2}}{1-e^{ik_y}}e_1(\vec{k}). \quad \text{(A33)}$$

The $k_x=0$ and $k_y=0$ components of the displacements correspond to rigid displacements, which are set to zero:

$$u^x_{k_x=0,k_y=0}=0, \quad \text{(A34)}$$

$$u^y_{k_x=0,k_y=0}=0. \quad \text{(A35)}$$

By adding periodic and nonperiodic parts of displacements according to Eqs. (A1) and (A2), we find $u^x_{\vec{i}}$ and $u^y_{\vec{i}}$.

APPENDIX B: ENERGY EXPRESSIONS FOR INHOMOGENEOUS STATES

To study inhomogeneous configurations, particularly metastable configurations, we minimize E_{tot} analytically with respect to all the independent variables except $s_x(\vec{i})$ and $s_y(\vec{i})$, that is, $e_1(\vec{k}=0)$, $e_2(\vec{k}=0)$, $e_3(\vec{k}=0)$, $e_1(k_x=0,k_y\neq 0)=-e_3(k_x=0,k_y\neq 0)$, $e_2(k_x=0,k_y\neq 0)$, $e_1(k_x\neq 0,k_y=0)=e_3(k_x\neq 0,k_y=0)$, and $e_2(k_x\neq 0,k_y=0)$, and we obtain an energy expression $E'_{\mathrm{tot}}(s_x,s_y)$. The details of the derivation are as follows. First, we represent e_1, e_2, and e_3 in reciprocal space, and we rewrite

E_l and E_c in Eqs. (3) and (4) in the following form:

$$E_l = N^2 \sum_{\vec{k}} \frac{A_1}{2} e_1(\vec{k}) e_1(-\vec{k}) + \frac{A_2}{2} e_2(\vec{k}) e_2(-\vec{k}) + \frac{A_3}{2} e_3(\vec{k}) e_3(-\vec{k}), \tag{B1}$$

$$E_c = \sum_{\vec{i}} \left\{ C_3 [s_x(\vec{i})^2 - s_y(\vec{i})^2] \sum_{\vec{k}} e_3(\vec{k}) e^{i\vec{k}\cdot\vec{i}} \right\}. \tag{B2}$$

Next, because the constraint equations apply differently depending on whether either k_x or k_y is zero or not, we divide the $\vec{k}$ sum into four parts,

$$\sum_{\vec{k}} = \sum_{k_x \neq 0, k_y \neq 0} + \sum_{k_x = 0, k_y \neq 0} + \sum_{k_x \neq 0, k_y = 0} + \sum_{k_x = 0, k_y = 0}, \tag{B3}$$

and we treat each part separately. If $k_x \neq 0$ and $k_y \neq 0$, constraint equations (A23)–(A25) are rewritten as follows:

$$(e_1)_{k_x \neq 0, k_y \neq 0} = -\frac{i}{\sqrt{2}} \left[\cot \frac{k_y}{2} s_x(\vec{k}) + \cot \frac{k_x}{2} s_y(\vec{k}) \right], \tag{B4}$$

$$(e_2)_{k_x \neq 0, k_y \neq 0} = -\frac{i}{\sqrt{2}} \left[\cot \frac{k_x}{2} s_x(\vec{k}) + \cot \frac{k_y}{2} s_y(\vec{k}) \right], \tag{B5}$$

$$(e_3)_{k_x \neq 0, k_y \neq 0} = -\frac{i}{\sqrt{2}} \left[\cot \frac{k_y}{2} s_x(\vec{k}) - \cot \frac{k_x}{2} s_y(\vec{k}) \right]. \tag{B6}$$

Therefore, the part with $k_x \neq 0$ and $k_y \neq 0$ for E_l in Eq. (B1) is expressed as

$$(E_l)_{k_x \neq 0, k_y \neq 0} = \frac{N^2}{2} \sum_{k_x \neq 0, k_y \neq 0} \begin{pmatrix} s_x \\ s_y \end{pmatrix}^T_{-\vec{k}} \begin{pmatrix} B_{xx} & B_{xy} \\ B_{xy} & B_{yy} \end{pmatrix}_{\vec{k}} \begin{pmatrix} s_x \\ s_y \end{pmatrix}_{\vec{k}}, \tag{B7}$$

where

$$B_{xx}(\vec{k}) = \frac{1}{2}(A_1 + A_3) \cot^2 \frac{k_y}{2} + \frac{1}{2} A_2 \cot^2 \frac{k_x}{2}, \tag{B8}$$

$$B_{yy}(\vec{k}) = \frac{1}{2}(A_1 + A_3) \cot^2 \frac{k_x}{2} + \frac{1}{2} A_2 \cot^2 \frac{k_y}{2}, \tag{B9}$$

$$B_{xy}(\vec{k}) = \frac{1}{2}(A_1 + A_2 - A_3) \cot \frac{k_x}{2} \cot \frac{k_y}{2}. \tag{B10}$$

Similarly, the part with $k_x \neq 0$ and $k_y \neq 0$ for E_c in Eq. (B2) is equivalent to

$$(E_c)_{k_x \neq 0, k_y \neq 0} = \sum_{\vec{i}} \left\{ C_3 [s_x(\vec{i})^2 - s_y(\vec{i})^2] \sum_{k_x \neq 0, k_y \neq 0} - \frac{i}{\sqrt{2}} \left[\cot \frac{k_y}{2} s_x(\vec{k}) - \cot \frac{k_x}{2} s_y(\vec{k}) \right] e^{i\vec{k}\cdot\vec{i}} \right\}. \tag{B11}$$

For the terms with $k_x = 0$ and $k_y \neq 0$, we apply the constraint equation $e_1(\vec{k}) + e_3(\vec{k}) = 0$ to eliminate $e_1(\vec{k})$ in E_l in Eq. (B1) and obtain

$$(E_l + E_c)_{k_x = 0, k_y \neq 0} = N^2 \sum_{k_x = 0, k_y \neq 0} \frac{A_1 + A_3}{2} e_3(-\vec{k}) e_3(\vec{k}) + \frac{A_2}{2} e_2(-\vec{k}) e_2(\vec{k}) + \sum_{\vec{i}} C_3 [s_x(\vec{i})^2 - s_y(\vec{i})^2] \sum_{k_x = 0, k_y \neq 0} e_3(\vec{k}) e^{ik_y i_y}. \tag{B12}$$

Since we are interested in metastable phases in this work and $e_2(\vec{k})$ and $e_3(\vec{k})$ are independent for $k_x = 0$ and $k_y \neq 0$, we minimize the energy $(E_l + E_c)_{k_x = 0, k_y \neq 0}$ with respect to $e_2(\vec{k})$ and $e_3(\vec{k})$ separately and obtain

$$(e_1)^{\min}_{k_x = 0, k_y \neq 0} = -(e_3)^{\min}_{k_x = 0, k_y \neq 0} = \frac{C_3 \mathcal{F}_{0,k_y}(s_x^2 - s_y^2)}{A_1 + A_3}, \tag{B13}$$

$$(e_2)^{\min}_{k_x = 0, k_y \neq 0} = 0, \tag{B14}$$

where

$$\mathcal{F}_{\vec{k}}(s_x^2 - s_y^2) \equiv \frac{1}{N^2} \sum_{\vec{i}} [s_x(\vec{i})^2 - s_y(\vec{i})^2] e^{-i\vec{k}\cdot\vec{i}}. \tag{B15}$$

The minimized energy expression for $(E_l + E_c)_{k_x = 0, k_y \neq 0}$ is

$$(E_l + E_c)^{\min}_{k_x = 0, k_y \neq 0} = -\frac{C_3^2}{2(A_1 + A_3)} N^2 \sum_{k_x = 0, k_y \neq 0} \mathcal{F}_{0,-k_y} \times (s_x^2 - s_y^2) \mathcal{F}_{0,k_y}(s_x^2 - s_y^2). \tag{B16}$$

We apply a similar analysis to the terms with $k_x \neq 0$ and $k_y = 0$ in Eqs. (B1) and (B2). Using the constraint $e_1(\vec{k}) - e_3(\vec{k}) = 0$, we eliminate $e_1(\vec{k})$ and obtain

$$(E_l + E_c)_{k_x \neq 0, k_y = 0} = N^2 \sum_{k_x \neq 0, k_y = 0} \frac{A_1 + A_3}{2} e_3(-\vec{k}) e_3(\vec{k}) + \frac{A_2}{2} e_2(-\vec{k}) e_2(\vec{k}) + \sum_{\vec{i}} C_3 [s_x(\vec{i})^2 - s_y(\vec{i})^2] \sum_{k_x \neq 0, k_y = 0} e_3(\vec{k}) e^{ik_x i_x}. \tag{B17}$$

Independent minimizations of this energy with respect to $e_2(\vec{k})$ and $e_3(\vec{k})$ lead to

$$(e_1)^{\min}_{k_x \neq 0, k_y = 0} = (e_3)^{\min}_{k_x \neq 0, k_y = 0} = -\frac{C_3 \mathcal{F}_{k_x,0}(s_x^2 - s_y^2)}{A_1 + A_3}, \tag{B18}$$

$$(e_2)^{\min}_{k_x \neq 0, k_y = 0} = 0, \tag{B19}$$

$$(E_l + E_c)^{\min}_{k_x \neq 0, k_y = 0} = -\frac{C_3^2}{2(A_1 + A_3)} N^2 \sum_{k_x \neq 0, k_y = 0} \mathcal{F}_{-k_x,0} \times (s_x^2 - s_y^2) \mathcal{F}_{k_x,0}(s_x^2 - s_y^2). \tag{B20}$$

The terms with $\vec{k} = 0$ in Eqs. (B1) and (B2) are

$$(E_l + E_c)_{k_x = 0, k_y = 0} = N^2 \left[\frac{A_1}{2} e_1(\vec{k} = 0)^2 + \frac{A_2}{2} e_2(\vec{k} = 0)^2 + \frac{A_3}{2} e_3(\vec{k} = 0)^2 \right] + \sum_{\vec{i}} C_3 [s_x(\vec{i})^2 - s_y(\vec{i})^2] e_3(\vec{k} = 0). \tag{B21}$$

We minimize the above expression with respect to $e_1(\vec{k}=0)$, $e_2(\vec{k}=0)$, and $e_3(\vec{k}=0)$ independently, since they are not constrained to each other, and we obtain

$$(e_1)^{\min}_{k_x=0,k_y=0} = 0, \tag{B22}$$

$$(e_2)^{\min}_{k_x=0,k_y=0} = 0, \tag{B23}$$

$$(e_3)^{\min}_{k_x=0,k_y=0} = -\frac{C_3}{A_3}\mathcal{F}_{\vec{k}=0}\left(s_x^2 - s_y^2\right), \tag{B24}$$

$$(E_l + E_c)^{\min}_{k_x=0,k_y=0} = -\frac{C_3^2 N^2}{2A_3}\left[\mathcal{F}_{\vec{k}=0}\left(s_x^2 - s_y^2\right)\right]^2. \tag{B25}$$

Finally, by adding the terms with different cases of k_x and k_y found above, we obtain the following total energy, $E'_{\rm tot}$, which depends only on s_x and s_y:

$$E'_{\rm tot}(s_x,s_y) = E'_{l+c} + E_s, \tag{B26}$$

where

$$E'_{l+c} = (E_l + E_c)^{\min}_{k_x=0,k_y=0} + (E_l + E_c)^{\min}_{k_x=0,k_y\neq 0} + (E_l + E_c)^{\min}_{k_x\neq 0,k_y=0} + (E_l)_{k_x\neq 0,k_y\neq 0} + (E_c)_{k_x\neq 0,k_y\neq 0}, \tag{B27}$$

and E_s is given by Eq. (2). We use this energy expression $E'_{\rm tot}(s_x,s_y)$ for the simulations of inhomogeneous states.

In addition to $s_x(\vec{i})$ and $s_y(\vec{i})$ configurations, $e_1(\vec{i})$, $e_2(\vec{i})$, and $e_3(\vec{i})$ configurations give useful information on the nature of the inhomogeneous states. The relations used to eliminate e_1, e_2, and e_3 variables above, namely Eqs. (B4)–(B6), (B13), (B14), (B18), (B19), and (B22)–(B24) for different cases of k_x and k_y, are used to find $e_1(\vec{k})$, $e_2(\vec{k})$, and $e_3(\vec{k})$ from given $s_x(\vec{i})$ and $s_y(\vec{i})$, which lead to $e_1(\vec{i})$, $e_2(\vec{i})$, and $e_3(\vec{i})$ configurations. Equations (A26)–(A35) are used to find the displacements, $u_x(\vec{i})$ and $u_y(\vec{i})$, from the distortion modes.

APPENDIX C: GRADIENTS OF THE ENERGY EXPRESSION FOR SIMULATIONS USING THE EULER METHOD

The gradient of $E'_{\rm tot}(s_x,s_y)$ necessary for the Euler method is found from

$$\frac{\partial E'_{\rm tot}(s_x,s_y)}{\partial s_x(\vec{i})} = \frac{\partial (E_l)^{k_y\neq 0}_{k_x\neq 0}}{\partial s_x(\vec{i})} + \frac{\partial (E_c)^{k_y\neq 0}_{k_x\neq 0}}{\partial s_x(\vec{i})} + \frac{\partial (E_l + E_c)^{\min}_{k_x=0,k_y\neq 0}}{\partial s_x(\vec{i})} + \frac{\partial (E_l + E_c)^{\min}_{k_x\neq 0,k_y=0}}{\partial s_x(\vec{i})} + \frac{\partial (E_l + E_c)^{\min}_{k_x=0,k_y=0}}{\partial s_x(\vec{i})} + \frac{\partial E_s}{\partial s_x(\vec{i})}, \tag{C1}$$

$$\frac{\partial E'_{\rm tot}(s_x,s_y)}{\partial s_y(\vec{i})} = \frac{\partial (E_l)^{k_y\neq 0}_{k_x\neq 0}}{\partial s_y(\vec{i})} + \frac{\partial (E_c)^{k_y\neq 0}_{k_x\neq 0}}{\partial s_y(\vec{i})} + \frac{\partial (E_l + E_c)^{\min}_{k_x=0,k_y\neq 0}}{\partial s_y(\vec{i})} + \frac{\partial (E_l + E_c)^{\min}_{k_x\neq 0,k_y=0}}{\partial s_y(\vec{i})} + \frac{\partial (E_l + E_c)^{\min}_{k_x=0,k_y=0}}{\partial s_y(\vec{i})} + \frac{\partial E_s}{\partial s_y(\vec{i})}. \tag{C2}$$

The expression for each term is given below:

$$\frac{\partial (E_l)_{k_x\neq 0,k_y\neq 0}}{\partial s_x(\vec{i})} = \sum_{k_x\neq 0,k_y\neq 0}\left[B_{xx}(\vec{k})s_x(\vec{k}) + B_{xy}(\vec{k})s_y(\vec{k})\right]e^{i\vec{k}\cdot\vec{i}}, \tag{C3}$$

$$\frac{\partial (E_l)_{k_x\neq 0,k_y\neq 0}}{\partial s_y(\vec{i})} = \sum_{k_x\neq 0,k_y\neq 0}\left[B_{yy}(\vec{k})s_y(\vec{k}) + B_{xy}(\vec{k})s_x(\vec{k})\right]e^{i\vec{k}\cdot\vec{i}}, \tag{C4}$$

$$\frac{\partial (E_c)_{k_x\neq 0,k_y\neq 0}}{\partial s_x(\vec{i})} = \frac{iC_3}{\sqrt{2}}\sum_{k_x\neq 0,k_y\neq 0}\left\{\cot\frac{k_y}{2}\mathcal{F}_{\vec{k}}\left(s_x^2 - s_y^2\right) - 2s_x(\vec{i})\left[\cot\frac{k_y}{2}s_x(\vec{k}) - \cot\frac{k_x}{2}s_y(\vec{k})\right]\right\}e^{i\vec{k}\cdot\vec{i}}, \tag{C5}$$

$$\frac{\partial (E_c)_{k_x\neq 0,k_y\neq 0}}{\partial s_y(\vec{i})} = \frac{iC_3}{\sqrt{2}}\sum_{k_x\neq 0,k_y\neq 0}\left\{\cot\frac{k_x}{2}\mathcal{F}_{\vec{k}}\left(s_y^2 - s_x^2\right) - 2s_y(\vec{i})\left[\cot\frac{k_x}{2}s_y(\vec{k}) - \cot\frac{k_y}{2}s_x(\vec{k})\right]\right\}e^{i\vec{k}\cdot\vec{i}}, \tag{C6}$$

$$\frac{\partial (E_l + E_c)^{\min}_{k_x=0,k_y\neq 0}}{\partial s_x(\vec{i})} = -\frac{2C_3^2}{A_1 + A_3}s_x(\vec{i})\sum_{k_x=0,k_y\neq 0}e^{ik_y i_y}\mathcal{F}_{0,k_y}\left(s_x^2 - s_y^2\right), \tag{C7}$$

$$\frac{\partial (E_l + E_c)^{\min}_{k_x=0,k_y\neq 0}}{\partial s_y(\vec{i})} = \frac{2C_3^2}{A_1 + A_3}s_y(\vec{i})\sum_{k_x=0,k_y\neq 0}e^{ik_y i_y}\mathcal{F}_{0,k_y}\left(s_x^2 - s_y^2\right), \tag{C8}$$

$$\frac{\partial (E_l + E_c)^{\min}_{k_x\neq 0,k_y=0}}{\partial s_x(\vec{i})} = -\frac{2C_3^2}{A_1 + A_3}s_x(\vec{i})\sum_{k_x\neq 0,k_y=0}e^{ik_x i_x}\mathcal{F}_{k_x,0}\left(s_x^2 - s_y^2\right), \tag{C9}$$

$$\frac{\partial (E_l + E_c)^{\min}_{k_x\neq 0,k_y=0}}{\partial s_y(\vec{i})} = \frac{2C_3^2}{A_1 + A_3}s_y(\vec{i})\sum_{k_x\neq 0,k_y=0}e^{ik_x i_x}\mathcal{F}_{k_x,0}\left(s_x^2 - s_y^2\right), \tag{C10}$$

$$\frac{\partial (E_l + E_c)^{\min}_{\vec{k}=0}}{\partial s_x(\vec{i})} = -\frac{2C_3^2}{A_3}s_x(\vec{i})\mathcal{F}_{\vec{k}=0}\left(s_x^2 - s_y^2\right), \tag{C11}$$

$$\frac{\partial (E_l + E_c)^{\min}_{\vec{k}=0}}{\partial s_y(\vec{i})} = \frac{2C_3^2}{A_3} s_y(\vec{i}) \mathcal{F}_{\vec{k}=0} \left(s_x^2 - s_y^2\right), \tag{C12}$$

$$\frac{\partial E_s}{\partial s_x(\vec{i})} = B s_x(\vec{i}) + G_1 s_x(\vec{i})^3 + G_2 s_x(\vec{i}) s_y(\vec{i})^2 + H_1 s_x(\vec{i})^5 + \frac{H_2}{3} [2 s_x(\vec{i})^2 + s_y(\vec{i})^2] s_x(\vec{i}) s_y(\vec{i})^2, \tag{C13}$$

$$\frac{\partial E_s}{\partial s_y(\vec{i})} = B s_y(\vec{i}) + G_1 s_y(\vec{i})^3 + G_2 s_y(\vec{i}) s_x(\vec{i})^2 + H_1 s_y(\vec{i})^5 + \frac{H_2}{3} [2 s_y(\vec{i})^2 + s_x(\vec{i})^2] s_y(\vec{i}) s_x(\vec{i})^2. \tag{C14}$$

*kenahn@njit.edu

†Present address: Department of Physics, Northern Illinois University, De Kalb, IL 60115, USA and Advanced Photon Source, Argonne National Laboratory, Argonne, IL 60439, USA.

[1] N. Mathur and P. Littlewood, Phys. Today **56**(1), 25 (2003).

[2] M. Uehara, S. Mori, C. H. Chen, and S.-W. Cheong, Nature (London) **399**, 560 (1999).

[3] Ch. Renner, G. Aeppli, B.-G. Kim, Y.-A. Soh, and S.-W. Cheong, Nature (London) **416**, 518 (2002).

[4] M. Fäth, S. Freisem, A. A. Menovsky, Y. Tomioka, J. Aarts, and J. A. Mydosh, Science **285**, 1540 (1999).

[5] V. Kiryukhin, New J. Phys. **6**, 155 (2004).

[6] A. Moreo, S. Yunoki, and E. Dagotto, Science **283**, 2034 (1999).

[7] J. Burgy, A. Moreo, and E. Dagotto, Phys. Rev. Lett. **92**, 097202 (2004).

[8] K. H. Ahn and T. Lookman, arXiv:cond-mat/0408077.

[9] J. Lorenzana, C. Castellani, and C. Di Castro, Europhys. Lett. **57**, 704 (2002); K. I. Kugel, A. L. Rakhmanov, A. O. Sboychakov, F. V. Kusmartsev, N. Poccia, and A. Bianconi, Supercond. Sci. Technol. **22**, 014007 (2009); V. B. Shenoy, T. Gupta, H. R. Krishnamurthy, and T. V. Ramakrishnan, Phys. Rev. B **80**, 125121 (2009).

[10] K. H. Ahn, T. Lookman, and A. R. Bishop, Nature (London) **428**, 401 (2004).

[11] K. H. Ahn, T. Lookman, and A. R. Bishop, J. Appl. Phys. **99**, 08A703 (2006).

[12] N. D. Mathur and P. B. Littlewood, Solid State Commun. **119**, 271 (2001).

[13] A. J. Millis, Solid State Commun. **126**, 3 (2003).

[14] A. R. Bishop, T. Lookman, A. Saxena, and S. R. Shenoy, Europhys. Lett. **63**, 289 (2003).

[15] N. Mathur, Nat. Mater. **5**, 849 (2006).

[16] M. Kim, H. Barath, S. L. Cooper, P. Abbamonte, E. Fradkin, M. Rübhausen, C. L. Zhang, and S.-W. Cheong, Phys. Rev. B **77**, 134411 (2008); T. A. Tyson, M. Deleon, M. Croft, V. G. Harris, C.-C. Kao, J. Kirkland, and S.-W. Cheong, *ibid.* **70**, 024410 (2004).

[17] L. Zhang, C. Israel, A. Biswas, R. L. Greene, and A. de Lozanne, Science **298**, 805 (2002).

[18] N. Mathur and P. Littlewood, Nat. Mater. **3**, 207 (2004).

[19] A. C. Mclaughlin, F. Sher, and J. P. Attfield, Nature (London) **436**, 829 (2005); R. P. Rairigh, G. Singh-Bhalla, S. Tongay, T. Dhakal, A. Biswas, and A. F. Hebard, Nat. Phys. **3**, 551 (2007); J. Cao, E. Ertekin, V. Srinivasan, W. Fan, S. Huang, H. Zheng, J. W. L. Yim, D. R. Khanal, D. F. Ogletree, J. C. Grossman, and J. Wu, Nat. Nanotech. **4**, 732 (2009); Y. Murakami, H. Kasai, J. J. Kim, S. Mamishin, D. Shindo, S. Mori, and A. Tonomura, *ibid.* **5**, 37 (2010); T.-H. Kim, M. Angst, B. Hu, R. Jin, X.-G. Zhang, J. F. Wendelken, E. W. Plummer, and A.-P. Li, Proc. Natl. Acad. Sci. (USA) **107**, 5272 (2010); K. Lai, M. Nakamura, W. Kundhikanjana, M. Kawasaki, Y. Tokura, M. A. Kelly, and Z.-X. Shen, Science **329**, 190 (2010); G. E. Ice, J. D. Budai, and J. W. L. Pang, *ibid.* **334**, 1234 (2011); A. Y. Borisevich, E. A. Eliseev, A. N. Morozovska, C.-J. Cheng, J.-Y. Lin, Y. H. Chu, D. Kan, I. Takeuchi, V. Nagarajan, and S. V. Kalinin, Nat. Commun. **3**, 775 (2012).

[20] D. D. Sarma, D. Topwal, U. Manju, S. R. Krishnakumar, M. Bertolo, S. La Rosa, G. Cautero, T. Y. Koo, P. A. Sharma, S.-W. Cheong, and A. Fujimori, Phys. Rev. Lett. **93**, 097202 (2004).

[21] J. Tao, D. Niebieskikwiat, M. B. Salamon, and J. M. Zuo, Phys. Rev. Lett. **94**, 147206 (2005).

[22] T. Z. Ward, J. D. Budai, Z. Gai, J. Z. Tischler, L. Yin, and J. Shen, Nat. Phys. **5**, 885 (2009).

[23] S. Semenovskaya, Y. Zhu, M. Suenaga, and A. G. Khachaturyan, Phys. Rev. B **47**, 12182 (1993).

[24] J. Slutsker, A. Artemev, and A. Roytburd, Phys. Rev. Lett. **100**, 087602 (2008).

[25] F. Nabarro, *Theory of Crystal Dislocations* (Clarendon, Oxford, 1967).

[26] http://web.njit.edu/~kenahn/programs.htm.

[27] M. B. Salamon and M. Jaime, Rev. Mod. Phys. **73**, 583 (2001).

[28] A. J. Millis, P. B. Littlewood, and B. I. Shraiman, Phys. Rev. Lett. **74**, 5144 (1995); H. Röder, J. Zang, and A. R. Bishop, *ibid.* **76**, 1356 (1996); A. J. Millis, B. I. Shraiman, and R. Mueller, *ibid.* **77**, 175 (1996); A. J. Millis, Nature (London) **392**, 147 (1998).

[29] S. Jin, T. H. Tiefel, M. McCormack, R. A. Fastnacht, R. Ramesh, and L. H. Chen, Science **264**, 413 (1994).

[30] G. C. Milward, M. J. Calderón, and P. B. Littlewood, Nature (London) **433**, 607 (2005).

[31] C. H. Chen and S.-W. Cheong, Phys. Rev. Lett. **76**, 4042 (1996).

[32] Y. Tokura, H. Kuwahara, Y. Moritomo, Y. Tomioka, and A. Asamitsu, Phys. Rev. Lett. **76**, 3184 (1996).

[33] H. Y. Hwang, S.-W. Cheong, P. G. Radaelli, M. Marezio, and B. Batlogg, Phys. Rev. Lett. **75**, 914 (1995).

[34] H. Y. Hwang, T. T. M. Palstra, S.-W. Cheong, and B. Batlogg, Phys. Rev. B **52**, 15046 (1995).

[35] V. Kiryukhin, D. Casa, J. P. Hill, B. Keimer, A. Vigliante, Y. Tomioka, and Y. Tokura, Nature (London) **386**, 813 (1997).

[36] V. Podzorov, B. G. Kim, V. Kiryukhin, M. E. Gershenson, and S.-W. Cheong, Phys. Rev. B **64**, 140406 (2001).

[37] T. Lookman, S. R. Shenoy, K. Ø. Rasmussen, A. Saxena, and A. R. Bishop, Phys. Rev. B **67**, 024114 (2003); T. Lookman and P. B. Littlewood, MRS Bull. **34**, 822 (2011).

[38] S. R. Shenoy, T. Lookman, A. Saxena, and A. R. Bishop, Phys. Rev. B **60**, R12537 (1999).

[39] K. H. Ahn, T. Lookman, A. Saxena, and A. R. Bishop, Phys. Rev. B **68**, 092101 (2003).

[40] X. Ren and K. Otsuka, MRS Bull. **27**, 116 (2011).

[41]K. Ø. Rasmussen, T. Lookman, A. Saxena, A. R. Bishop, R. C. Albers, and S. R. Shenoy, Phys. Rev. Lett. **87**, 055704 (2001).

[42]We note that because of the anisotropy, e.g., $\cos(4\theta)$ for the two-dimensional model in Ref. 38, the interaction is more convergent than for $1/r^D$.

[43]Although the results of two- and three-dimensional simulations are similar, three-dimensional simulations generally produce more complicated domain structures. For example, the three-dimensional simulations in Ref. 41 have produced helical twins as a result of orientational elastic frustration, not present in two-dimensional simulations.

[44]Y. Ono and T. Hamano, J. Phys. Soc. Jpn. **69**, 1769 (2000).

[45]For the electron hopping constant, electron-lattice coupling constant, and distortions with sizes similar to those for manganites, the SSH Hamiltonian results in a gap with a size similar to the gap in manganites, which further supports the validity of the SSH Hamiltonian for the current study.

[46]The distance between the nearest-neighbor atoms, a, is irrelevant to our formalism presented here, but it affects the figures, for which a is chosen as 10 Å, a value of the same order of magnitude as the nearest-neighbor Mn-Mn distance in manganites.

[47]A. O. Sboychakov, A. L. Rakhmanov, and K. I. Kugel, J. Phys.: Condens. Matter **22**, 415601 (2010).

[48]Furthermore, the formation of polarons, which is not considered in our model but is known to be important in manganites,[28] would also influence the phase coexistence.[47]

[49]K. H. Ahn, T. Lookman, A. Saxena, and A. R. Bishop, Phys. Rev. B **71**, 212102 (2005).

[50]Necessary conditions for such first-order-transition-like energy landscapes are $G_1' \equiv G_1 - 2C_3^2/A_3 < 0$ and $(G_1')^2 > 4BH_1$, for which the energy minima occur at $(\tilde{s}_x,\tilde{s}_y) = (0,0)$, $(\pm s_0,0)$, and $(0,\pm s_0)$ with $s_0 = \sqrt{[-G_1' + \sqrt{(G_1')^2 - 4BH_1}]/(2H_1)}$.

[51]The local energy minimum states with the opposite signs of $\tilde{s}_x$ or $\tilde{s}_y$ are related by a phase difference of the short-wavelength distortion, whereas the local energy minimum states along the $\tilde{s}_x$ axis are related to those along the $\tilde{s}_y$ axis by an exchange of the x and y axes.

[52]K. H. Ahn and A. J. Millis, Phys. Rev. B **64**, 115103 (2001).

[53]N. Poccia, A. Ricci, and A. Bianconi, J. Supercond. Nov. Magn. **24**, 1195 (2010).

[54]P. A. Sharma, S. B. Kim, T. Y. Koo, S. Guha, and S.-W. Cheong, Phys. Rev. B **71**, 224416 (2005).

[55]W. Wu, C. Israel, N. Hur, S. Park, S.-W. Cheong, and A. de Lozanne, Nat. Mater. **5**, 881 (2006).

[56]A small mistake has been found in the code used for Ref. 10, which is corrected here, responsible for minor differences between Figs. 4(a)–4(d) and the corresponding figures in Ref. 10.

[57]The parameters W, X, and Y are chosen to be identical to the parameters B, G_1', and H_1 in units of eV/Å^2, eV/Å^4, and eV/Å^6 for the lattice model. We choose $Z = 5$, similar to A_1, A_2, and A_3 in the unit of eV/Å^2, since $e_1(\vec{i})$, $e_2(\vec{i})$, and $e_3(\vec{i})$ are related to the gradient of $s_x(\vec{i})$ and $s_y(\vec{i})$ in the continuum limit.[39]

[58]The Euler simulation has been carried out with $\gamma = 0.000\,15$. The configurations at the Euler step, $n = 10\,000$ and $40\,000$, and the final stable configuration at $n = 1\,000\,000$ are shown in Figs. 4(f)–4(h).

[59]M. Fiebig, K. Miyano, Y. Tomioka, and Y. Tokura, Science **280**, 1925 (1998).

[60]S. R. Shenoy and T. Lookman, Phys. Rev. B **78**, 144103 (2008); R. Vasseur and T. Lookman, *ibid.* **81**, 094107 (2010); Solid State Phenom. **172–174**, 1078 (2010).